

Field-Particle Interactions in Curved Flows for Shape-Asymmetric Active Particles

Derek C. Gomes^{1,*} and Tapan C. Adhyapak^{1,†}

¹*Department of Physics, Indian Institute of Science Education and Research (IISER) Tirupati, Tirupati, Andhra Pradesh, 517619, India*

We show that curvatures in general ambient flow profiles can align shape-asymmetric active particles, revealing a previously overlooked competition with externally applied aligning fields. Focusing on the ubiquitous case of channel flows, we then investigate the fundamental consequences of this competition for the dynamics of shape-asymmetric active particles in microchannels in the presence of orienting fields. We find that this interplay gives rise to novel mechanisms for controlling particle dynamics, with potentially broad applications, and suggests exciting possibilities such as active-particle analogs of electronic systems.

Control of active particle dynamics through externally applied orienting fields is of considerable interest due to their broad technological and biological applications [1, 2]. While several studies have demonstrated successful field coupling to active particles [3–7], the absence of an adequate theoretical framework has limited both the scope and development of experimental techniques.

In this paper, we show that in curved flows, head-tail shape-asymmetric (HT-A) particles experience polar aligning torques arising from a competition between local flow curvatures in different planes. We investigate the interplay between this flow-curvature-induced alignment and externally applied orienting fields in the presence of activity, revealing dynamics of HT-A microswimmers that differ strikingly from those of head-tail symmetric (HT-S) swimmers and HT-A swimmers without external fields. Our results demonstrate surprisingly simple ways to tune microswimmer dynamics across a wide range of dynamical states.

Several studies have demonstrated field-based control of active-particle dynamics, both in quiescent and imposed flows [8–13]. Many living microswimmers, including both pullers and pushers [14], possess intrinsic [3, 4, 15] or engineered [16] dipole moments that couple to external conjugate fields. Moreover, work on aligning synthetic microswimmers with external fields is receiving significant thrust [17–21]. When such field aligning active particles are subjected to flow environments, they display striking phenomena. These include, for *e.g.* vertical migration [8] and dense layering of microswimmers in oceans [22], bio-convective pattern formation [23–25], externally controllable particle density profiles [5], and even Bose-Einstein-like condensation in microswimmers [26]. However, all the above works focus on HT-S properties without exploring HT-A specific effects. The flow-curvature induced HT-A alignments, in these systems, may become dominant in unexplored setups and deserves further investigations.

The dynamics of both passive and active particles in flow have been formulated using the Jeffery equation [27, 28]. This equation, however, implicitly considers only HT-S particles and their resulting HT-S interactions

with flow. While HT-A active particles/microswimmers, such as *E. coli* and *B. subtilis*, are both ubiquitous as well as bio-technologically relevant [29, 30], their dynamics in the literature continue to be analyzed using the Jeffery equation [31, 32], thereby approximating them as HT-S, for simplicity. Our recent work [33] however, demonstrates that effect of HT-A on flow-particle interactions can be non-trivial, and whose signatures may have already been reported but not sufficiently inspected [31]. While our equation is valid for general flows, we consider Poiseuille flow to illustrate the dynamical consequences of flow and field competition, due to the central role of this flow in natural [34–36] and technological [37, 38] contexts.

We show that, under suitable conditions, HT-S swimmers in Poiseuille flow and an aligning field can be focused to any desired height, and not just the flow mid-plane or channel walls, as reported earlier [5]. Moreover, while the effect of two competing field sources on particle dynamics has been recently reported [6], we show that with imposed flows added they can cause interesting dynamics with potentially broad applications. We then show that with just a single field source and in imposed flows, HT-A swimmers can also converge to a *stable limit cycle*, producing constant-period, constant-frequency oscillations in their trajectory, tuned by the applied field. Varying the field strength can drive these HT-A specific dynamics to transition into those seen for HT-S swimmers, through at least four sharp *bifurcations*, offering additional controls.

Our study begins with a prototypical model of an HT-A particle, which we later generalize to arbitrary HT-A shapes. The model comprises a spherical cell body with a slender flagellar rod, developed in [33]. The sphere center \mathbf{r}_s and orientation $\hat{\mathbf{n}}$ evolve according to $d\mathbf{r}_s/dt = \mathbf{v}_s$ and $d\hat{\mathbf{n}}/dt = \boldsymbol{\omega}^{\text{flow}} \times \hat{\mathbf{n}}$, once the translational and angular velocities \mathbf{v}_s and $\boldsymbol{\omega}^{\text{flow}}$, respectively, are determined.

Extending the formulation outlined in Ref. [33], using the force and torque balance conditions for a low Reynolds number swimmer, we attain the translational and rotational velocities \mathbf{v}_s and $\boldsymbol{\omega}^{\text{flow}}$, respectively, in terms of a general ambient flow $\mathbf{u}^0(\mathbf{r})$, in

the limit of an infinitely rigid flagellar rod. This flow contains finely resolved hydrodynamics, including image fields that capture flow reflections off the cell-body [33, 39, 40]. Coupling the leading order gradients of the flow [upto $\mathcal{O}(\nabla \nabla \mathbf{u}^0)$] to the swimmer background, and initially considering planar dynamics $\mathbf{r}_s = (x, y)$ and $\hat{\mathbf{n}} = (\cos \theta, \sin \theta)$, the velocities become:

$$\dot{x} = v^{\text{sp}} \cos \theta - r_{\text{sh}} \dot{\theta} \sin \theta + \mathbf{v}_s^{\text{drift}} \cdot \hat{\mathbf{x}}, \quad (1)$$

$$\dot{y} = v^{\text{sp}} \sin \theta + r_{\text{sh}} \dot{\theta} \cos \theta + \mathbf{v}_s^{\text{drift}} \cdot \hat{\mathbf{y}}, \quad (2)$$

$$\begin{aligned} \dot{\theta} = \frac{1}{2} \{ & (\nabla_s \times \mathbf{u}_s^0) \cdot \hat{\mathbf{z}} \\ & + \beta_2 [\cos 2\theta E_{s,xy}^0 + \sin 2\theta (E_{s,yy}^0 - E_{s,xx}^0)] \\ & + (\beta_1 \sin \theta + \beta_3 \sin^3 \theta) \nabla_s^2 u_s^0 \} \end{aligned} \quad (3)$$

Here x is along the local flow direction $\hat{\mathbf{u}}^0(\mathbf{r})$, y is perpendicular to x and the flow vorticity direction and θ is the angle between $\hat{\mathbf{n}}$ and $\hat{\mathbf{u}}^0(\mathbf{r})$. v^{sp} is the particle self-propulsion speed, r_{sh} is the displacement of \mathbf{r}_s , along $\hat{\mathbf{n}}$, from the hydrodynamic center \mathbf{r}_h , about which the swimmer rotates. The particle drift due to flow, $\mathbf{v}_s^{\text{drift}} = -\ell_f \{ 6\pi\eta a \{ \rho_{\parallel} \hat{\mathbf{n}} \hat{\mathbf{n}} + \rho_{\perp} [\mathbf{I} - \hat{\mathbf{n}} \hat{\mathbf{n}}] \} + \rho_{\parallel} \rho_{\perp} \ell_f \mathbf{I} \} \cdot \hat{\mathbf{u}}_s^0 \times \{ a^2 \nabla^2 u_s^0 / 6 + (a + \ell_f / 2) (\hat{\mathbf{n}} \cdot \nabla) u_s^0 - (a^2 + a\ell_f + \ell_f^2 / 3) \times (\hat{\mathbf{n}} \cdot \nabla) (\hat{\mathbf{n}} \cdot \nabla) u_s^0 / 2 \} / (6\pi\eta a + \rho_{\parallel} \ell_f) (6\pi\eta a + \rho_{\perp} \ell_f)$,

where η is the fluid viscosity, a the cell-body radius, ℓ_f the appendage length and $(\rho_{\parallel}, \rho_{\perp})$ the friction per unit length along and perpendicular to the appendage long axis, respectively. Throughout, the subscript s refers to the evaluation of the respective field quantity at $\mathbf{r} = \mathbf{r}_s$. $E_{s,ij}^0 = (\nabla_i u_{s,j}^0 + \nabla_j u_{s,i}^0) / 2$, is the local strain-rate tensor.

Note that, for Poiseuille flow, the plane (y, x) is well defined by the shear plane, and Eq. (1) decouples from Eqs. (2) and (3), and the latter two exactly map to the equations in [33]. For dynamics evaluated about $\mathbf{r}_h = \mathbf{r}_s - r_{\text{sh}} \hat{\mathbf{n}}$ instead of \mathbf{r}_s , $\dot{\theta}$ drops out of the x, y dynamics, while the following variables transform as $(x, y) \rightarrow (\tilde{x}, \tilde{y})$ and hence $(\beta_1, \beta_3) \rightarrow (\tilde{\beta}_1, \tilde{\beta}_3)$, where $\tilde{x} = x + r_{\text{sh}} \cos \theta$, $y \rightarrow y + r_{\text{sh}} \sin \theta$, $\beta_1 \rightarrow \beta_1 - (1 - \beta_2) r_{\text{sh}}$ and $\beta_3 \rightarrow \beta_3 - 2\beta_2 r_{\text{sh}}$. The orientation $\hat{\mathbf{n}}$, its angular velocity ω , and β_2 , remain unchanged.

The planar dynamics of Eqs. (1)-(3), generalized to full three-dimensions, and now about \mathbf{r}_h , become: $\dot{\mathbf{r}}_h = v^{\text{sp}} \hat{\mathbf{n}} + \mathbf{v}_h^{\text{drift}}$ and $\dot{\hat{\mathbf{n}}} = \omega^{\text{flow}} \times \hat{\mathbf{n}}$, where $\mathbf{v}_h^{\text{drift}}$ is the same as $\mathbf{v}_s^{\text{drift}}$, but with derivatives in its expression now w.r.t \mathbf{r}_h , and \mathbf{u}_s^0 replaced by $\mathbf{u}_h^0 + r_{\text{sh}} (\hat{\mathbf{n}} \cdot \nabla_h) \mathbf{u}_h^0 + r_{\text{sh}}^2 (\hat{\mathbf{n}} \cdot \nabla_h) (\hat{\mathbf{n}} \cdot \nabla_h) \mathbf{u}_h^0 / 2$, and the angular velocity,

$$\omega^{\text{flow}} = \frac{1}{2} \nabla_h \times \mathbf{u}_h^0 + \beta_2 \hat{\mathbf{n}} \times \mathbf{E}_h^0 \cdot \hat{\mathbf{n}} + \tilde{\beta}_1 \hat{\mathbf{n}} \times \nabla_h^2 \mathbf{u}_h^0 + \tilde{\beta}_3 \hat{\mathbf{n}} \times (\hat{\mathbf{n}} \cdot \nabla_h) (\hat{\mathbf{n}} \cdot \nabla_h) \mathbf{u}_h^0. \quad (4)$$

The subscript h now denotes the field quantity evaluated at $\mathbf{r} = \mathbf{r}_h$. Note that, the $\tilde{\beta}_1$ and $\tilde{\beta}_3$ terms in Eq. (4) are not captured in the Jeffery equation [27, 28], since the latter equation is only upto first order in gradients. However, the last two terms in (4), unlike the first two, cause ω^{flow} to change when $\hat{\mathbf{n}} \rightarrow -\hat{\mathbf{n}}$, and are hence new asymmetric terms, thus not ignorable.

Further, on phenomenological grounds, the asymmetric terms above are the only ones that can couple the orientation $\hat{\mathbf{n}}$ to gradients of the flow \mathbf{u}^0 , upto second order (Fig. 1a-ii) while yielding a vector contribution to ω^{flow} orthogonal to $\hat{\mathbf{n}}$, *i.e.*, excluding rotation about particle axis $\hat{\mathbf{n}}\hat{\mathbf{n}}$. For shape-*symmetric* particles, symmetry forbids such asymmetric dynamics, implying $\tilde{\beta}_1, \tilde{\beta}_3 = 0$, a result confirmed for our model swimmer in the limit of vanishing appendage size [33]. This justifies the truncation of the Jeffery equation upto first order in gradients (Fig. 1a-i), but only for shape-symmetric particles.

For shape-asymmetric particles, Eq. (4) is therefore the natural extension of the Jeffery equation for angular velocity, containing the leading order asymmetric terms. We also suggest Eq. (4) must hold for *any* uniaxial particle with a shape asymmetry along that axis that interacts with fluid flows. The structure of the last two

terms shows that flow gradients tend to align $\hat{\mathbf{n}}$ either along or against the local flow direction $\hat{\mathbf{u}}_h^0$, depending on the signs of $\tilde{\beta}_1$ and $\tilde{\beta}_3$ (see Fig. 1b). This provides additional insight into the results of [33] and indicates that such *flow-alignment* may compete with other field-induced alignments, generating new dynamics.

The tendency of many microswimmers to reorient toward external fields—light, gravity, electric, or magnetic [15, 41]—can be attributed to an aligning torque of the form $\mathbf{T}_f = p \hat{\mathbf{n}} \times \mathbf{E}_f$, where $p \hat{\mathbf{n}}$ is an effective dipole moment and \mathbf{E}_f the field it couples to. Including such field alignment modifies the angular velocity to $\omega = \omega^{\text{flow}} + \omega^{\text{field}}$, with $\omega^{\text{field}} = \bar{E} \hat{\tau}$, $\hat{\tau} = \hat{\mathbf{n}} \times \mathbf{E}_f / |\hat{\mathbf{n}} \times \mathbf{E}_f|$, and $\bar{E} = p |\mathbf{E}_f| / \gamma_R$, where γ_R is the effective rotational friction of the particle.

In Fig. 1c, we illustrate the competition between flow and field by evaluating ω^{flow} for a particle at $y = 0$ in Poiseuille flow and taking θ_0 , the angle made by \mathbf{E}_f with the flow direction, as π , as an example. For large deviations from upstream ($\theta = \pi$; main panel), the flow contribution $\dot{\theta} = \omega^{\text{flow}} \cdot \hat{\mathbf{z}}$ (blue) destabilizes the upstream orientation, while for field $\dot{\theta} = \omega^{\text{field}} \cdot \hat{\mathbf{z}}$ (yellow) stabilizes it. Near $\theta = \pi$ (inset), both contributions stabilize the upstream orientation. The HT-A parameters considered,

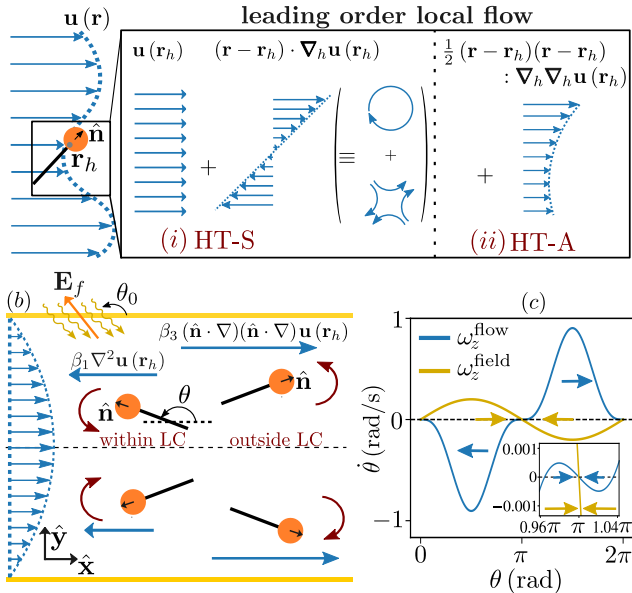


FIG. 1. *Polar alignments from flow and fields:* (a) Flow $\mathbf{u}(\mathbf{r})$ expanded about the hydrodynamic center \mathbf{r}_h of an HT-A swimmer oriented along $\hat{\mathbf{n}}$. Leading-order rotational and straining flows [(i)] generate Jeffery-type, $\hat{\mathbf{n}} \rightarrow -\hat{\mathbf{n}}$ symmetric rotations, whereas second-order gradients [(ii)] break this symmetry. (b) Steady orientations arise from four contributions: flow vorticity (maroon), polar alignment to the field \mathbf{E}_f (orange), flow-induced polar alignment $\propto \beta_1, \beta_3$ along/against the local flow (blue), and apolar alignment $\propto \beta_2$ along the straining axis [cf. (a) – (i)]. (c) Contribution to $\dot{\theta} \equiv \omega_z$ from the flow (blue) and the field (yellow) plotted function of θ for Poiseuille flow at $y = 0, \theta_0 = \pi$ and $\bar{E} = 0.2$. *Inset:* zoom near $\theta = \pi$.

$\beta_{1,2,3}$ and r_{sh} ($= 0.75a$), match those in [33].

Having obtained the general flow- and field-alignment terms with respect to \mathbf{r}_h , we now specialize to Poiseuille flow and express the dynamics again in terms of \mathbf{r}_s , maintaining convention [33]. Adding the field alignment, $\dot{\theta} = \boldsymbol{\omega} \cdot \hat{\mathbf{z}}$, the expressions in Eqs. (2) and (3) considering leading order hydrodynamics, become:

$$\dot{y} = v^{sp} \sin \theta - r_{sh} \dot{\theta} \cos \theta + \frac{\ell_f (\rho_{\parallel} - \rho_{\perp}) f(y, \theta)}{\gamma_{\parallel} \gamma_{\perp}}, \quad (5)$$

$$\dot{\theta} = \frac{v_f}{R^2} [(1 - \beta_2) y + 2\beta_2 \sin^2 \theta y + \beta_1 \sin \theta + \beta_3 \sin^3 \theta] - \bar{E} \sin(\theta - \theta_0). \quad (6)$$

Here, the x - dynamics gets decoupled from y, θ , and is deferred to Appendix, along with the expression for $f(y, \theta)$. Next, $\gamma_{\parallel(\perp)} = 1 + \rho_{\parallel(\perp)} \ell_f / 6\pi \eta a$, v_f and R are the maximum flow speed and channel radius, respectively, as Poiseuille flow, $\mathbf{u}_{s, \text{Poiseuille}}^0 = v_f (1 - y^2/R^2) \hat{\mathbf{x}}$. Note (\bar{E}, θ_0) are the additional parameters due to field-alignment, and are both tunable without modifying the particle.

For numerical analysis, we take $v^{sp} = 50 \mu\text{m/s}$, $v_f = 500 \mu\text{m/s}$, $R = 50 \mu\text{m}$, while the values of β_1, β_2 and

β_3 are taken from their expressions given in [33], with $a = 1 \mu\text{m}$, $\ell_f = 5 \mu\text{m}$, and $(\eta, \rho_{\parallel}, \rho_{\perp}) = (0.89, 3.9, 6.7) \times 10^{-3} \text{ Pa-s}$. This gives $\beta_1 > 0, 0 < \beta_2 < 1$, while $\beta_3 < 0$. The parameter $r_{sh} = 0.75a$, taken to incorporate the effects of detailed active flows on the location of \mathbf{r}_h (see [33]). Finally, the $\{\dot{x}, \dot{y}, \dot{\theta}\}$ equations are integrated numerically via Euler integration with timestep $dt = 5 \times 10^{-5} \text{ s}$, to attain $\{x(t), y(t), \theta(t)\}$.

HT-S particle dynamics— When $\ell_f = 0$, our particle becomes HT-S, as $\beta_{1,3}$ and $r_{sh} = 0$ (additionally $\beta_2 = 0$ as our cell-body is spherical). Applying a field \mathbf{E}_f at various θ_0 and strengths \bar{E} , we recover the results of [5, 26]: trajectories focus to the centerline in an upstream orientation for an upstream source ($\theta_0 = \pi$) and spread toward the walls for a downstream source ($\theta_0 = 0$). We further find that for $\pi/2 < \theta_0 < 3\pi/2$ (but $\theta_0 \neq \pi$), particles can instead focus at intermediate heights. For $-\pi/2 < \theta_0 < \pi/2$ with $\theta_0 \neq 0$, particles spread to the boundaries, with more trajectories approaching the wall from the side of field incidence (Fig. 1b). Fig. 2a shows representative cases for $\theta_0 = 3\pi/4$ and $\theta_0 = \pi/4$ with $\bar{E} = 6$. Fig. 2b illustrates that symmetric field sources leads to particles moving along centerline, by symmetry, and hence detected (top), while removing one source leads to no detections, due to particle focusing at another height, y_{DC} (bottom), enabling a transistor-like switching response.

HT-A particle dynamics— HT-A particles ($\beta_{1,2,3}$ and $r_{sh} \neq 0$) behave strikingly differently from their HT-S counterparts. Fig. 2c shows HT-A trajectories at $\theta_0 = 3\pi/4$ for field strengths \bar{E}_1 to \bar{E}_4 . In addition to trajectories that settle to a fixed height (DC), we find ones that oscillate across the centerline with fixed amplitude and frequency (AC) and others that migrate towards the walls (H).

The above implies that in a dilute suspension of HT-A swimmers, the total population may consist of subpopulations of DC, AC and H trajectories. We define n_{DC} , n_{AC} and n_H as the fraction of swimmers in the above three subpopulations, respectively. From this, we define a normalized current density $\bar{J}_\alpha = J_\alpha / v_x$, where α is either DC, AC or H and $J_\alpha = n_\alpha \langle v_x \rangle$, with $\langle v_x \rangle$ the average particle velocity along the flow direction, here $\hat{\mathbf{x}}$.

The typical HT-A dynamics are summarized in Fig. 2c. For large field strengths, $\bar{E} = \bar{E}_1 = 1.2$, HT-A particles focus at a single height y_{DC} , giving only \bar{J}_{DC} . When \bar{E} falls below a first critical value $\bar{E}_{C,1} \approx 0.51$, an AC component \bar{J}_{AC} appears alongside \bar{J}_{DC} , with a reduced y_{DC} , as shown for $\bar{E}_2 = 0.5$. Below a second critical threshold $\bar{E}_{C,2} \approx 0.36$, the wall-directed component $\bar{J}_{H,\uparrow}$ emerges, corresponding to trajectories moving toward the field source (seen for $\bar{E}_3 = 0.3$). Finally, when \bar{E} drops below $\bar{E}_{C,3} \approx 0.29$, \bar{J}_{AC} disappears, leaving \bar{J}_{DC} , $\bar{J}_{H,\uparrow}$, and a component directed toward the opposite boundary, $\bar{J}_{H,\downarrow}$, shown for $\bar{E}_4 = 0.2$. By definition,

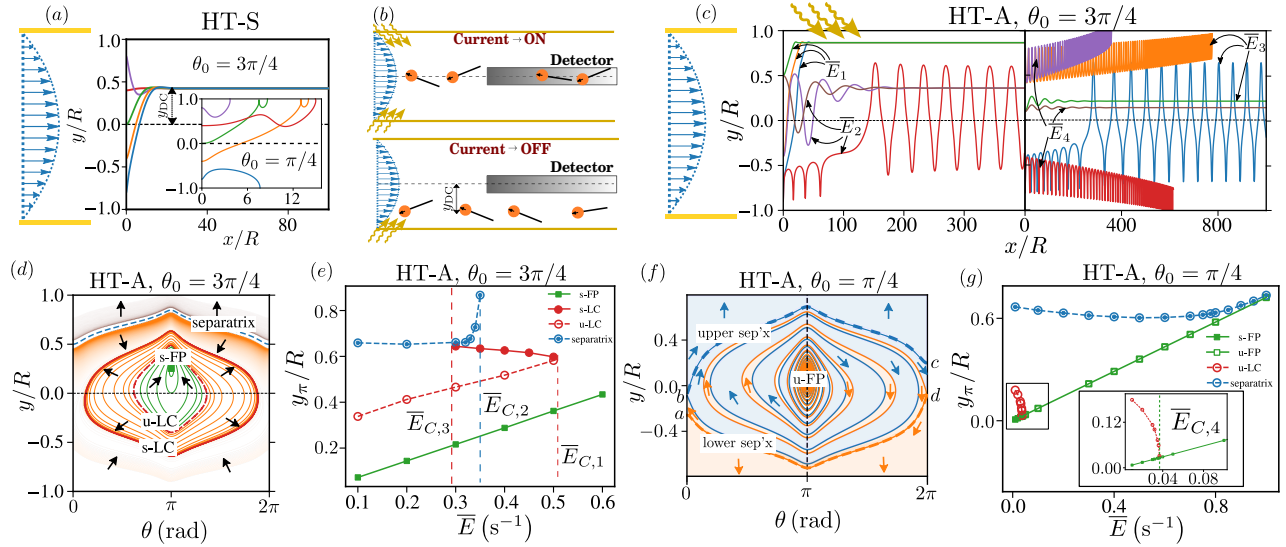


FIG. 2. (a) **HT-S dynamics:** Trajectories for different initial heights y_i at $\theta_i = \pi$ with a field at $\theta_0 = 3\pi/4$. Inset: Same y_i, θ_i for $\theta_0 = \pi/4$. (b) Schematic of HT-S/HT-A particles with two symmetric field sources on (top) and with only one source on (bottom). (c) **HT-A dynamics:** (Left panel) Trajectories for two different field strengths \bar{E}_1, \bar{E}_2 , with three y_i common to both \bar{E} , (Right panel) Trajectories for \bar{E}_3, \bar{E}_4 , with a another set of three common y_i . $\bar{E}_1 > \dots > \bar{E}_4$. All have $\theta_i = \pi$. (d) Phase space at $\theta_0 = 3\pi/4$ ($\bar{E} = 0.35$), showing the stable fixed point (s-FP, green), unstable limit cycle (u-LC, dashed red), stable limit cycle (s-LC, filled red), and separatrix (blue). (e) Corresponding y_π values of the s-FP, u-LC, s-LC, and separatrix vs. \bar{E} , at $\theta = \pi$, with arrows indicating effective trajectory directions. (f) Phase space at $\theta_0 = \pi/4$ ($\bar{E} = 0.35$), showing the unstable fixed point (u-FP) and separatrix (blue). Initial conditions starting at blue regions end up at the top wall; orange regions to the bottom. {a, b} are the starting and {d, c} are the ending points of the {lower,upper} separatrix. (g) Corresponding y_π vs. \bar{E} plot at $\theta_0 = \pi/4$.

$$\bar{J}_H = \bar{J}_{H,\uparrow} + \bar{J}_{H,\downarrow} [42].$$

For the other representative orientation, $\theta_0 = \pi/4$, we find that over a wide range of \bar{E} all particles move toward one wall or the other, yielding only \bar{J}_H , similar to the HT-S case. However, when \bar{E} falls below a critical value, $\bar{E}_{C,4} \approx 0.04$, a fraction of trajectories instead focus to a fixed height near the centerline ($y_{DC} \ll R$), constituting a \bar{J}_{DC} (see Appendix).

The dynamics for all initial conditions are understood via the phase space (y, θ). Figure 2d shows this space for $\bar{E} = 0.35$ at $\theta_0 = 3\pi/4$. A separatrix (dashed blue) divides trajectories: those starting above it reach the top wall, those below are confined within the separatrix. Inside the separatrix lie a stable limit cycle (s-LC, filled red), an unstable limit cycle (u-LC, dashed red), and a stable fixed point (s-FP, green). Initial conditions inside the u-LC approach the FP, while those inside the separatrix but outside the u-LC approach the s-LC. Thus, for a large non-interacting population uniformly distributed in phase space, the area inside the u-LC gives $n_{DC} = \bar{J}_{DC}$, the area inside the separatrix but outside the u-LC gives $n_{AC} = \bar{J}_{AC}$, and the area outside the separatrix gives $n_{H,\uparrow} = \bar{J}_{H,\uparrow}$. When an additional separatrix exists near the lower wall (see Appendix), the phase-space region between the lower separatrix and the lower wall yields $n_{H,\downarrow} = \bar{J}_{H,\downarrow}$.

Next, we examine how the phase space changes with

\bar{E} , for a particular $\theta_0 = 3\pi/4$, summarized in Fig. 2e. This figure shows y_π , the y -coordinates of the separatrix, s-LC, u-LC, and s-FP at $\theta = \pi$, as a function of \bar{E} . For large \bar{E} , only the s-FP exists. At $\bar{E} = \bar{E}_{C,1}$, a s-LC+u-LC pair appears (**fold bifurcation**). As \bar{E} is lowered further, y_π of the s-LC increases and that of the u-LC decreases, both nonlinearly, while that of the s-FP decreases linearly. At $\bar{E} = \bar{E}_{C,2}$, the separatrix first emerges at the wall, and its y_π then decreases with decreasing \bar{E} . At $\bar{E} = \bar{E}_{C,3}$, the y_π values of the separatrix and s-LC coincide, eliminating the s-LC (**homoclinic-like bifurcation**). For $\bar{E} < \bar{E}_{C,3}$, only the separatrix, u-LC, and s-FP remain.

The phase space for $\theta_0 = \pi/4$ and $E > \bar{E}_{C,4}$ (Fig. 2f) contains an unstable fixed point (u-FP) bounded by two separatrices. Initial conditions above or below these separatrices go to the top (blue) or bottom (orange) walls [43]. Points between the separatrices also divide into blue and orange regions leading to the corresponding walls.

The y_π vs. \bar{E} variation for $\theta_0 = \pi/4$ is shown in Fig. 2g. For large \bar{E} , the separatrix and u-FP share similar y_π but decreasing \bar{E} causes y_π of the u-FP to fall linearly, while that of the separatrix decreases, reaches a minimum, and then rises. At $\bar{E} = \bar{E}_{C,4}$, the u-FP becomes a s-FP+u-LC pair at the same y_π (**subcritical Hopf bifurcation**). For $E < \bar{E}_{C,4}$, with decreasing \bar{E}

the y_π of u-LC increases nonlinearly, while that of the s-FP decreases approximately linearly.

The particle currents defined above for both HT-S and HT-A particles are shown in Fig. 3. For HT-S, the behavior is simple: $\bar{J}_{DC} = 1$ for $\pi/2 < \theta_0 < 3\pi/2$, and $\bar{J}_H = 1$ for $-\pi/2 < \theta_0 < \pi/2$. Representative cases for $\theta_0 = 3\pi/4$ and $\pi/4$ are plotted in Fig. 3a.

For HT-A at $\theta_0 = 3\pi/4$, the current at large \bar{E} ($> \bar{E}_{C,1}$) matches the HT-S result, with $\bar{J}_{DC} = 1$. At low \bar{E} ($< \bar{E}_{C,3}$), though still at $\theta_0 = 3\pi/4$, resembles HT-S at $\theta_0 = \pi/4$, but with a small nonzero \bar{J}_{DC} and hence a sub-unity, though dominant, \bar{J}_H . In the intermediate regime, $\bar{E}_{C,3} < \bar{E} < \bar{E}_{C,1}$, the current is instead dominated by \bar{J}_{AC} , which peaks at $\bar{E} = \bar{E}_{C,2}$. Thus, HT-A display richer current variations than HT-S, with sharp transitions at critical \bar{E} values, summarized in Fig. 3b.

In the Appendix, we further decompose \bar{J}_H into its upward ($\bar{J}_{H,\uparrow}$) and downward ($\bar{J}_{H,\downarrow}$) contributions as \bar{E} varies. For $\theta_0 = \pi/4$, HT-A particles behave identically to HT-S when $\bar{E} > \bar{E}_{C,4}$, yielding $\bar{J}_H = 1$. For $\bar{E} < \bar{E}_{C,4}$, \bar{J}_H decreases slightly, allowing a small but finite \bar{J}_{DC} to appear (see Appendix).

We now explain our findings. For Poiseuille flow, Eqs. (2) and (6) admit a fixed point (FP) $\{y_{FP}, \theta_{FP}\} = \{\bar{E} \sin \theta_0 R^2 / (1 - \beta_2) v_f, \pi\}$, among others (see Supplemental Material). We show later that this FP is linearly stable for all \bar{E} at $\theta_0 = 3\pi/4$, for both HT-S and HT-A parameters. Since $\theta_{FP} = \pi$, y_{FP} is precisely the y_π of the s-FP, and the analytical expression matches the numerically obtained y_π for both HT-S and HT-A. Moreover, y_{FP} (equivalently y_π and the DC focusing height y_{DC}) decreases linearly with decreasing \bar{E} , consistent with the phenomenology discussed earlier.

To analyse dynamics around the FP, we eliminate y from (6), using (5) and replace θ by its deviation from the FP: $\psi = \theta - \theta^{FP}$. By expanding the resulting equation upto fifth order in ψ , we get:

$$\ddot{\psi} + k_1 \psi = \zeta_m \psi^m \dot{\psi} + (\mu_3 \psi + \mu_5 \psi^3) \dot{\psi}^2 + k_n \psi^n, \quad (7)$$

where $m = 0 \rightarrow 4$ and $n = 3, 4, 5$. This equation is similar to the modified van der Pol Equation (vdPE) in [33], but additionally contains even powers of combinations of $\psi, \dot{\psi}$ due to vertical component of the field $\bar{E} \sin \theta_0$, which provide $\cos \theta$ contributions to $\dot{\theta}$ (see Eq. 6). The horizontal field component $\bar{E} \cos \theta_0$ provides $\sin \theta$ terms which therefore contribute similarly to the β_1 terms in the $\dot{\theta}$ and ultimately $\dot{\psi}$ equation. The $\mathcal{O}(\psi^5)$ terms are retained here as their influence grows with field strength, as shown later.

The expressions for all parameters in Eq. (7) are given in the Supplemental Material. The damping coefficient, $\mu_1 = \bar{E} \cos \theta_0 - [\beta_1 + (1 - \beta_2) r_{sh}] v_f / R^2$ governs the linear stability of the FP. For small ψ , Eq (7) yields relaxation to $\psi = 0$ when $\mu_1 < 0$, implying that both $\theta^{FP} = \pi$ and y^{FP} are linearly stable; for $\mu_1 > 0$ the FP is unstable.

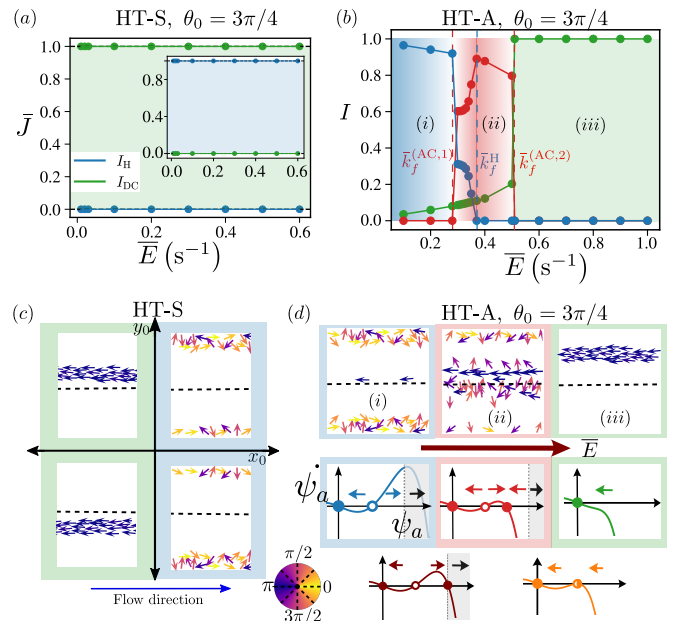


FIG. 3. Implications for swimmer populations. (a) HT-S particle currents \bar{J}_H (blue dot) and \bar{J}_{DC} (green dot) vs. \bar{E} for $\theta_0 = 3\pi/4$; background color reflects the dominant current. Inset: corresponding currents for $\theta_0 = \pi/4$. (b) HT-A currents for $\theta_0 = 3\pi/4$, showing the emergence of \bar{J}_{AC} (red) in regime (ii) between regimes dominated by \bar{J}_H (blue) and \bar{J}_{DC} (green). (c) Schematic HT-S concentration profiles and orientations for different field incidence angles θ_0 across the (x_0, y_0) quadrants; arrow colors encode deviation of orientation from upstream ($\theta = \pi$). (d) Top: Schematic HT-A population states for $\theta_0 = 3\pi/4$, corresponding to regimes (i) – (iii) in panel b. Middle: Theoretically obtained $\psi_a - \psi_a$ curves, indicating stability directions (colored arrows). The region beyond the separatrix is shaded gray with black arrows showing its instability. Bottom: $\psi_a - \psi_a$ curves showing (left) the merger of separatrix and stable limit cycle (brown filled dot+gray region), and (right) the formation of a half-stable limit cycle (orange half-filled circle).

For HT-S particles ($\beta_{1,2} = 0, r_{sh} = 0$), $\mu_1 = \bar{E} \cos \theta_0$, so the FP is stable only when $\cos \theta_0 < 0$ ($\pi/2 < \theta_0 < 3\pi/2$) and unstable otherwise. These stability ranges reproduce exactly the focusing and wall-going regimes of HT-S swimmers.

For HT-A swimmers, the additional $\beta_{1,2}$ and r_{sh} terms allow μ_1 to change sign even at fixed θ_0 , giving a critical $\bar{E}_{\mu_1=0} = v_f [\beta_1 + (1 - \beta_2) r_{sh}] / \cos \theta_0 R^2$. This predicts the subcritical bifurcation observed at $\theta_0 = \pi/4$, for which $\bar{E}_{\mu_1=0}(\theta_0 = \pi/4) = \bar{E}_{C,4} = \sqrt{2} v_f [\beta_1 + (1 - \beta_2) r_{sh}] / R^2$. Using the coefficients from the Supplemental Material gives $\bar{E}_{C,4} \approx 0.037$, matching our simulations.

More generally, the subcritical bifurcation exists for any θ_0 whenever $\bar{E} = \bar{E}_{\mu_1=0}$. However, for $\pi/2 < \theta_0 < 3\pi/2$, where $\cos \theta_0 < 0$, $\bar{E}_{\mu_1=0}$ requires $\bar{E} < 0$ for our parameters, which is equivalent to $\cos \theta_0, \bar{E} > 0$. Thus no such bifurcation occurs in this θ_0 range, where the FP remains stable for all $\bar{E} > 0$.

Stable LC emergence — for small values of $\mu_1/\sqrt{k_1}$, $\zeta_l/\sqrt{\zeta_2^l}$, $\mu_m/\sqrt{\zeta_2^{m-1}}$, $k_n/k_1\sqrt{\zeta_2^{n-1}}$, for $l = 1, 3, 4$, $m = 3, 5$ and $n = 3 \rightarrow 5$, which are all $\sim \mathcal{O}(\mu_1/\sqrt{k_1})$, $\psi(t) \approx \psi_a(\mu_1 t) \cos [\sqrt{k_1}t + \phi(\mu_1 t)]$. Here ψ_a and ϕ are the amplitude and phase of the oscillating solution that vary on a slower timescale $\mu_1 t$ compared to $\sqrt{k_1}t$. From Averaging theory [44], we get the equation for the amplitude as:

$$\dot{\psi}_a = -\frac{\zeta_2 \mu_1}{8} \left(\frac{4}{\zeta_2} \psi_a - \psi_a^3 + \frac{1}{2} \zeta_4 \zeta_2 \psi_a^5 \right). \quad (8)$$

Here ζ_4 depends on \bar{E} in addition to $\beta_{1,2,3}$ and r_{sh} (see Supplemental Material), so the ψ_a^5 term in Eq. (8) can become significant for certain \bar{E} , unlike the $\bar{E} = 0$ case. The resulting $\dot{\psi}_a$ - ψ_a curves are shown in Fig. 3. For $\zeta_4 > \zeta_4^C = 0.5$, (e.g., $\zeta_4 = 2$, green curve, middle panel), the only solution is the stable FP at $\psi_a = 0$, corresponding to $(y_{\text{FP}}, \theta_{\text{FP}})$. At $\zeta_4 = \zeta_4^C$ (orange curve, bottom panel), an additional half-stable fixed point appears, implying a half-stable limit cycle that seeds the s-LC+u-LC pair. This proves the fold bifurcation at $\bar{E} = \bar{E}_{C,1}$, where $\zeta_4(\bar{E}_{C,1}) = \zeta_4^C$. For $\zeta_4 < \zeta_4^C$ (e.g., $\zeta_4 = 0.4$, red curve, middle panel), a stable and unstable FP exists for $\psi_a \neq 0$, corresponding to the s-LC and u-LC, producing the phase portrait of Fig. 2d and equivalently the AC current \bar{J}_{AC} shown in Fig. 3b.

When \bar{E} decreases from $\bar{E}_{C,2}$ to $\bar{E}_{C,3}$ (reducing ζ_4), the separatrix moves downward while the s-LC grows, the latter reflected in the increasing nonzero root of $\dot{\psi}_a = 0$. At $\bar{E} = \bar{E}_{C,3}$ these two collide, as seen by the merger of the gray region with the filled brown point in Fig. 3d (bottom panel), annihilating the s-LC. For $\bar{E} < \bar{E}_{C,3}$, the FP associated with this s-LC would lie beyond the separatrix and is therefore removed by higher-order nonlinearities omitted in our analytical approximation but captured by the full numerical dynamics. Consequently, only the s-FP, u-LC, and separatrix remain for $\bar{E} < \bar{E}_{C,3}$. The case $\bar{E} = 0$ studied in [33] belongs to this regime, which is why an expansion of $\psi, \dot{\psi}$ up to $\mathcal{O}(\psi^3)$ was sufficient there: such truncation eliminates the FP corresponding to s-LC at the very outset.

Conclusion — To summarize, we derived the flow-coupled dynamics of a *general* shape-asymmetric (HT-A) particle, yielding a generalized Jeffery equation [Eq. (4)]. We then examined how this dynamics is affected by an orienting field. In Poiseuille flow with a field, HT-S particles—previously known to focus at the midplane for upstream fields ($\theta_0 = \pi$)—can in fact be focused to arbitrary heights for other field angles. Fig. 3c provides schematic representations of the height and orientation distributions of swimmer populations across different field incidence angles θ_0 .

For HT-A particles, decreasing the field strength \bar{E} produces qualitatively new steady states. In particular, particles can also oscillate at a *single*, field-selected am-

plitude and frequency about the midplane, forming a *stable limit cycle* rather than focusing. The top panel of Fig. 3d schematizes these HT-A states for $\theta_0 = 3\pi/4$. Importantly, these behaviors change *abruptly* across specific critical field strengths. Our phenomenology identifies four such critical values, $\{\bar{E}_{C,1}, \bar{E}_{C,2}, \bar{E}_{C,3}, \bar{E}_{C,4}\}$, some of which we further established analytically.

We remark that for HT-A dynamics, the stable limit cycle can even arise without an external field, but at different values of the shape-asymmetric parameter β_1 . This follows from the expression for ζ_4 (see Supplemental Material), which governs the fold bifurcation in Eq. (8) and contains $v_f \beta_1 / R^2$ and $\bar{E} \cos \theta_0$ on equal footing. Both terms generate $\sin \theta$ contributions to $\dot{\theta}$ [see Eq. (6)], explaining why HT-A particles without a field exhibit dynamics similar to HT-S particles in a field, while also displaying features unique to shape asymmetry (due to β_3), such as coexisting stable and unstable limit cycles. The orienting field \bar{E} , however, provides an externally tunable control parameter that allows access to the wide range of states reported here without altering particle properties. Activity is essential, as it converts asymmetric angular velocities into particle currents. Apart from the β_1, β_3 terms, a weak instantaneous drift also contributes to dynamics perpendicular to the flow [see last term, Eq. (2)].

We have thus inferred novel signatures of shape-asymmetry, thereby opening new ways to characterize and sort swimmers based on their asymmetry. Our results suggest the possibility of creating electronic analogs with active particles (see, for *e.g.* Fig. 2b), while serving as an important first step towards the study of continuum dynamics of suspensions of shape-asymmetric active particles [45].

Acknowledgments — TCA acknowledges grants CRG/2021/004759 from the Science and Engineering Research Board (India) and MoE-STARS/STARS-2/2023-0814 for financial support. DCG acknowledges PMRF, Govt. of India, for fellowship and funding. TCA and DCG express gratitude to the *Indian Institute of Science Education and Research (IISER) Tirupati* for funds and facilities. Furthermore, the support and the resources provided by ‘PARAM Brahma Facility’ under the National Supercomputing Mission, Government of India at the *Indian Institute of Science Education and Research (IISER) Pune* are gratefully acknowledged.

* derekgomes@students.iisertirupati.ac.in

† Author to whom correspondence should be addressed: adhyapak@labs.iisertirupati.ac.in

[1] M. Zhao, B. Song, J. Pu, T. Wada, B. Reid, G. Tai, F. Wang, A. Guo, P. Walczysko, Y. Gu, *et al.*, Electrical signals control wound healing through phosphatidylinositol-3-oh kinase- γ and pten, *Nature (London)* **442**, 457 (2006).

[2] C. Copos, Y.-H. Sun, K. Zhu, Y. Zhang, B. Reid, B. Draper, F. Lin, H. Yue, Y. Bernadskaya, M. Zhao, *et al.*, Galvanotactic directionality of cell groups depends on group size, *Proc. Natl. Acad. Sci.* **122**, e2416440122 (2025).

[3] R. Blakemore, Magnetotactic bacteria, *Science* **190**, 377 (1975).

[4] T. J. Pedley and J. O. Kessler, Hydrodynamic phenomena in suspensions of swimming microorganisms, *Annual Review of Fluid Mechanics* **24**, 313 (1992).

[5] X. Garcia, S. Rafaï, and P. Peyla, Light control of the flow of phototactic microswimmer suspensions, *Phys. Rev. Lett.* **110**, 138106 (2013).

[6] S. Raikwar, A. Al-Kassem, N. S. Gov, A. I. Pesci, R. Jeanneret, and R. E. Goldstein, Phototactic decision-making by microalgae, *Phys. Rev. Lett.* **135**, 228401 (2025).

[7] P. Chong, B. Erable, and A. Bergel, How bacteria use electric fields to reach surfaces, *Biofilm* **3**, 100048 (2021).

[8] J. O. Kessler, Hydrodynamic focusing of motile algal cells, *Nature (London)* **313**, 218 (1985).

[9] L. Jibuti, L. Qi, C. Misbah, W. Zimmermann, S. Rafaï, and P. Peyla, *Phys. Rev. E* **90**, 063019 (2014).

[10] J. Arlt, V. A. Martinez, A. Dawson, T. Pilizota, and W. C. K. Poon, Painting with light-powered bacteria, *Nat. Commun.* **9**, 768 (2018).

[11] Y. Huang, A. Xia, G. Yang, and F. Jin, Bioprinting living biofilms through optogenetic manipulation, *ACS Synth. Biol.* **7**, 1195 (2018).

[12] A. Bricard, J.-B. Caussin, N. Desreumaux, O. Dauchot, and D. Bartolo, Emergence of macroscopic directed motion in populations of motile colloids, *Nature (London)* **503**, 95 (2013).

[13] W. Shi, B. Stocker, and J. Adler, Effect of the surface composition of motile escherichia coli and motile salmonella species on the direction of galvanotaxis, *J. Bacteriol.* **178**, 1113 (1996).

[14] M. C. Marchetti, J. F. Joanny, S. Ramaswamy, T. B. Liverpool, J. Prost, M. Rao, and R. A. Simha, Hydrodynamics of soft active matter, *Rev. Mod. Phys.* **85**, 1143 (2013).

[15] E. Lauga, *The Fluid Dynamics of Cell Motility*, Vol. 62 (Cambridge University Press, UK, 2020).

[16] M. Aubry, W.-A. Wang, Y. Guyodo, E. Delacou, J.-M. Guigner, O. Espeli, A. Lebreton, F. Guyot, and Z. Gueroui, Engineering e. coli for magnetic control and the spatial localization of functions, *ACS Synth. Biol.* **9**, 3030 (2020).

[17] C. M. Buness, A. Rana, C. C. Maass, and R. Dey, Electrotaxis of self-propelling artificial swimmers in microchannels, *Phys. Rev. Lett.* **133**, 158301 (2024).

[18] C. Lozano, B. ten Hagen, H. Löwen, and C. Bechinger, Phototaxis of synthetic microswimmers in optical landscapes, *Nat. Commun.* **7**, 12828 (2016).

[19] B. Dai, J. Wang, Z. Xiong, Z. Li, Z. Li, J. Tang, and X. Yang, Programmable artificial phototactic microswimmer, *Nat. Nanotechnol.* **11**, 1087 (2016).

[20] B. Ren *et al.*, Assembly behavior of iron oxide-capped janus particles in a magnetic field, *Langmuir* **28**, (2012).

[21] N. Yu, X. Lou, K. Chen, and M. Yang, Phototaxis of active colloids by self-thermophoresis, *Soft Matter* **15**, 408 (2019).

[22] W. M. Durham, J. O. Kessler, and R. Stocker, Disruption of vertical motility by shear triggers formation of thin phytoplankton layers, *Science* **323**, 1067 (2009).

[23] T. J. Pedley, N. Hill, and J. O. Kessler, The growth of bioconvection patterns in a uniform suspension of gyro-tactic micro-organisms, *J. Fluid Mech.* **195**, 223 (1988).

[24] J. Arrieta, M. Polin, R. Saleta-Piersanti, and I. Tuval, Light control of localized photobioconvection, *Phys. Rev. Lett.* **123**, 158101 (2019).

[25] C. Williams and M. Bees, Photo-gyrotactic bioconvection, *J. Fluid Mech.* **678**, 41 (2011).

[26] F. Meng, D. Matsunaga, B. Mahault, and R. Golestanian, Magnetic microswimmers exhibit bose-einstein-like condensation, *Phys. Rev. Lett.* **126**, 078001 (2021).

[27] G. B. Jeffery, The motion of ellipsoidal particles immersed in a viscous fluid, *Proc. R. Soc. Lond. Ser. A* **102**, 161 (1922).

[28] F. P. Bretherton, The motion of rigid particles in a shear flow at low reynolds number, *J. of Fluid Mech.* **14**, 284 (1962).

[29] H. C. Berg, *E. coli in Motion*, Biological and Medical Physics, Biomedical Engineering (Springer, 2004).

[30] X. Zhang, A. Al-Dossary, M. Hussain, P. Setlow, and J. Li, Applications of bacillus subtilis spores in biotechnology and advanced materials, *Applied and Environmental Microbiology* **86**, e01096 (2020).

[31] G. Junot, N. Figueroa-Morales, T. Darnige, A. Lindner, R. Soto, H. Auradou, and E. Clément, Swimming bacteria in poiseuille flow: The quest for active bretherton-jeffery trajectories, *EPL* **126**, 44003 (2019).

[32] D. Saintillan, Rheology of active fluids, *Annu. Rev. Fluid Mech.* **50**, 563 (2018).

[33] D. C. Gomes and T. C. Adhyapak, Shape asymmetry and flexibility in active cross-stream migration in nonuniform shear, *Phys. Rev. Lett.* **135**, 054001 (2025).

[34] J. L. M. Poiseuille, Recherches expérimentales sur le mouvement des liquides dans les tubes de très petits diamètres, *Comptes Rendus Hebdomadaires des Séances de l'Académie des Sciences* **11**, 961 (1840).

[35] Y. C. Fung, *Biomechanics: Circulation*, 2nd ed. (Springer, New York, 1997).

[36] M. T. Tyree and M. H. Zimmermann, *Xylem Structure and the Ascent of Sap*, 2nd ed. (Springer, Berlin, 2002).

[37] T. M. Squires and S. R. Quake, Microfluidics: Fluid physics at the nanoliter scale, *Rev. Mod. Phys.* **77**, 977 (2005).

[38] H. A. Stone, A. D. Stroock, and A. Ajdari, Engineering flows in small devices, *Annu. Rev. Fluid Mech.* **36**, 381 (2004).

[39] T. C. Adhyapak and S. Jabbari-Farouji, Flow properties and hydrodynamic interactions of rigid spherical microswimmers, *Phys. Rev. E* **96**, 052608 (2017).

[40] T. C. Adhyapak and S. Jabbari-Farouji, Ewald sum for hydrodynamic interactions of rigid spherical microswimmers, *J. Chem. Phys.* **149**, 144110 (2018).

[41] D. Das and D. Saintillan, Electrohydrodynamic interaction of spherical particles under quincke rotation, *Phys. Rev. E* **87**, 043014 (2013).

[42] We do not adopt the convention $J_H = |J_{H,\uparrow} - J_{H,\downarrow}|$.

[43] With minor exceptions in a narrow \overline{E} range; see Supplemental Material.

[44] S. H. Strogatz, *Nonlinear dynamics and chaos: with applications to physics, biology, chemistry, and engineering* (CRC press, 2018).

[45] D. C. Gomes and T. C. Adhyapak, (to be published).